SANDIA REPORT
SAND2017-10257
Unlimited Release
Printed September 2017

Compact Models for Defect Diffusivity in Semiconductor Alloys

A. F. Wright, N. A. Modine, S. R. Lee, and S. M. Foiles

Prepared by
Sandia National Laboratories
Albuquerque, New Mexico 87185

Sandia National Laboratories is a multimission laboratory managed and operated by National Technology and Engineering Solutions of Sandia LLC, a wholly owned subsidiary of Honeywell International Inc. for the U.S. Department of Energy's National Nuclear Security Administration under contract DE-AC04-94AL85000.

Sandia National Laboratories

Issued by Sandia National Laboratories, operated for the United States Department of Energy by National Technology and Engineering Solutions of Sandia LLC.

SAND2017-10257
Unlimited Release
Printed 9/2017

Compact Models for Defect Diffusivity in Semiconductor Alloys

A. F. Wright,[1] N. A. Modine,[1] S. R. Lee,[2] and S. M. Foiles[3]
[1] Nanostructure Physics Department
[2] Advanced Materials Sciences Department
[3] Computational Materials and Data Science Department
Sandia National Laboratories
P.O. Box 5800
Albuquerque, New Mexico 87185

Abstract

Predicting transient effects caused by short-pulse neutron irradiation of electronic devices is an important part of Sandia's mission. For example, predicting the diffusion of radiation-induced point defects is needed within Sandia's Qualification Alternative to the Sandia Pulsed Reactor (QASPR) program since defect diffusion mediates transient gain recovery in QASPR electronic devices. Recently, the semiconductors used to fabricate radiation-hard electronic devices have begun to shift from silicon to III-V compounds such as GaAs, InAs, GaP and InP. An advantage of this shift is that it allows engineers to optimize the radiation hardness of electronic devices by using alloys such as InGaAs and InGaP. However, the computer codes currently being used to simulate transient radiation effects in QASPR devices will need to be modified since they presume that defect properties (charge states, energy levels, and diffusivities) in these alloys do not change with time. This is not realistic since the energy and properties of a defect depend on the types of atoms near it and, therefore, on its location in the alloy. In particular, radiation-induced defects are created at nearly random locations in an alloy and the distribution of their local environments – and thus their energies and properties – evolves with time as the defects diffuse through the alloy. To incorporate these consequential effects into computer codes used to simulate transient radiation effects, we have developed procedures to accurately compute the time dependence of defect energies and properties and then formulate them within *compact models* that can be employed in these computer codes. In this document, we demonstrate these procedures for the case of the highly mobile P interstitial (I_P) in an InGaP alloy.

ACKNOWLEDGMENTS

This work was funded under LDRD Project Number 180932 and Title "Compact Models for Defect Diffusivity in Semiconductor Alloys."

CONTENTS

FIGURES

1. INTRODUCTION

In neutron irradiated semiconductor devices, both thermally-activated and carrier-induced processes may contribute to the diffusion of (point) defects produced by the irradiation. In thermally-activated (thermal) diffusion, a defect in a fixed charge state, *q,* hops between stable-state configurations over energy barriers associated with intervening saddle-point configurations, and the diffusion rate thus depends on these barriers and the temperature of the device. In carrier-induced diffusion, a change in a defect charge state upon capture or emission of a carrier is accompanied by a change in the (atomic) configuration of the defect. For example, in GaP (and InP) the stable-state configuration of the (q =) 0 P interstitial (I_P) is C_{2v} 110p, the stable-state configuration of the +1 I_P is C_{1h} p001g and each configurations converts into the other when a carrier is captured or emitted. Since each configuration is adjacent to two symmetrically equivalent locations of the other configuration, they form a network in GaP (and InP) such that repeated changes in the I_P charge state can produce diffusion without energy barriers with a diffusion rate that depends on the currents in the device.

In an InGaP alloy, these two diffusion processes are modified because the energy of I_P depends strongly on the occupation of nearby group-III sites, and thus on its location in the alloy. Thermal diffusion is biased toward more energetically favorable locations of I_P. Since net diffusion requires moving away from these locations, the effective barrier for diffusion will increase with time and eventually I_P may become trapped at its lowest-energy locations. Similarly, alloying breaks the symmetries that enable I_P to convert into two symmetric locations upon capture or emission a carrier. I_P undergoing carrier-induced diffusion may then encounter two neighboring sites that reliably convert into each other and become trapped at these sites. Fortunately, the combination of thermal and carrier-induced diffusion can enable I_P to escape the traps associated with each process taken individually. Thus, some amount of carrier capture can enhance thermal I_P diffusion, and vice versa.

A consequence of the trapping noted above is that thermal diffusion rate of I_P in InGaP decreases after a short time in contrast to the constant rate observed for I_P in GaP and InP. This decrease is illustrated in Fig. 1 where we plot results from our detailed study of thermal diffusion of -1 I_{As} in an $In_{0.5}Ga_{0.5}As$ alloy. This study employed Density-Functional Theory (DFT) to calculate I_{As} stable-state and saddle-point energies in a *training set* of alloy configurations, the Cluster Expansion (CE) approach to develop parameterized models of the I_{As} training-set energies that can be used to rapidly calculate I_{As} stable-state and saddle-point energies at arbitrary sites in the alloy, and Kinetic Monte-Carlo (KMC) to simulate I_{As} diffusion using the CEs. (See SAND2014-17844 for a detail discussion of this model, which we hereinafter refer to this as the DFT/CE/KMC model.) To highlight the decrease in the I_{As} diffusion rate, the time axis in the plot has been scaled relative to a virtual crystal approximation (VCA) in which E_B is the composition-weighted energy barrier for I_{As} diffusion in the alloy. As can be seen in the plot, the initial diffusion rates (the slopes of the plots) are the same as the rate for the VCA, but decrease after a short time period. Further analysis of the KMC results confirms that the decrease is due to I_{As} trapping at low-energy sites, which is mitigated with increasing temperature such that the diffusion rate approaches the VCA rate at high temperatures. We note that the existence of a short transient in the diffusion rate of a defect in an alloy (i.e., the short time period during which the defect diffuses rapidly before entering a slower, trap-mediated diffusion mode) may be important because: (1) such transients are difficult to detect in experiments and (2) a transient in the diffusion rate can produce a corresponding transient in the gain-recovery rate of a device during which the device may not operate correctly.

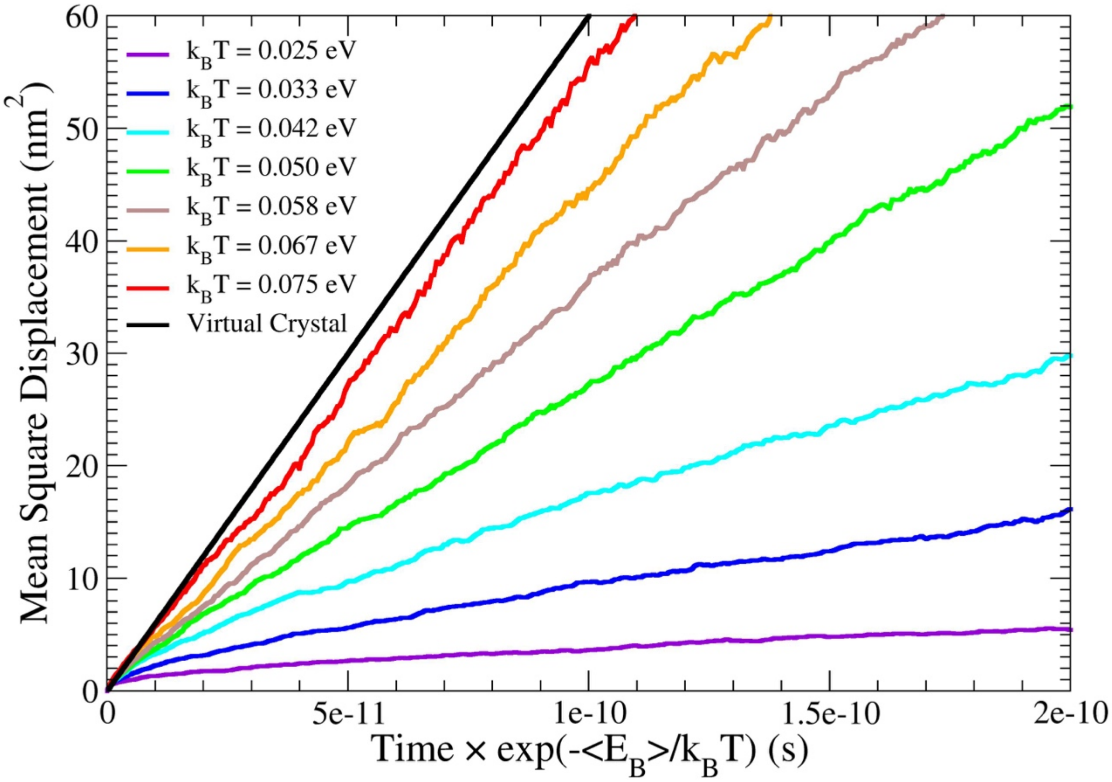

Figure 1. DFT/CE/KMC modeling results for thermal diffusion of -1 I_{As} in an InGaAs alloy at various temperatures. To highlight the decrease in the diffusion rate, the time axis has been scaled relative to a virtual-crystal approximation.

Although the DFT/CE/KMC model can yield accurate predictions of the time-dependent behavior of defects in alloys, it would be computationally prohibitive to directly incorporate it into the diffusion-reaction codes currently in use at Sandia to simulate radiation effects in semiconductor devices. Thus, the main objective of this LDRD is to develop a capability to extract *compact models* from the detailed results from the DFT/CE/KMC model and use these models in Sandia diffusion-reaction codes to assess the effects of this behavior on device operation. To prototype this capability, we have considered the case of I_P in an $In_{0.5}Ga_{0.5}P$ alloy (hereinafter referred to simply as InGaP), which is used in the emitter of an NPN QASPR heterojunction bipolar transistor (HBT). Following up on our discussion of the transient in the diffusion rates of defects in alloys, we note that the length scale of the mean-squared-displacement (MSD) during this transient will be one of the parameters in our compact model.

Below, we discuss our development of a DFT/CE/KMC model for I_P in InGaP and compact models extracted from this model. In Section 2, we detail our DFT calculations for I_P in training sets for three different charge states, including CEs for both their stable-state and saddle-point configurations. In Section 3, we describe the development and verification of CEs from the DFT results for these training sets. In Section 4, we describe the KMC results obtained using these CEs, both for thermal diffusion and combined thermal and carrier-induced diffusion. In Section 5, we discuss the compact models we extracted from the KMC results.

2. DENSITY-FUNCTIONAL THEORY

2.1 General Aspects of DFT Defect Calculations

In semiconductors, the defects produced by neutron irradiation may have multiple charge states, and transitions between these charge states yield (thermodynamic) defect levels which are the Fermi levels at which the transitions occur. Defect levels are technologically important because they may control the relative rates of carrier capture and emission, and thereby degrade the performance of a minority-carrier device. Moreover, the device performance may undergo additional changes as the defects diffuse and react with other defects, dopants and impurities. Measurements of defect levels are challenging, and using experiments to determine the atomistic origin of a level can require a lifetime of work. Because of this, there is considerable interest in theoretical studies of defects.

Most theoretical defect studies in semiconductors rely on Kohn-Sham DFT,[1,2] a semilocal exchange-correlation functional,[1,3,4] and norm-conserving pseudopotentials (NCPs).[5] DFT defect calculations are typically performed in a periodically repeated parallelpiped (supercell), containing a single defect surrounded by bulk material. The defect charge state, *q*, is modeled by adding or removing electrons from the supercell, and a uniform compensating charge distribution with integrated charge equal to $-q$ is added to the supercell so that the Poisson equation has a well-defined solution.[6] For a given charge state, two types of calculations may be needed: 1) A calculation of the stable configuration (the energy minimum with respect to small atomic displacements), and 2) a calculation of the saddle-point configuration that mediates thermal diffusion between adjacent stable configurations. Finding a stable configuration may involve both relaxation of the atomic coordinates for a particular configuration and comparison of different configurations. Saddle-point configurations are found using the dimer method,[7] and may also involve comparison of different configurations.

Once the stable and saddle-point configurations are found, their formation energies can be computed using the general-purpose expression [8]

$$E_f^D\left(q,L,E_F\right)=E^D\left(q,L\right)-E^B\left(0,L\right)-\Sigma_i n_i\,\mu_i+qE_F\,, \tag{1}$$

in which $E^D(q,L)$ is the energy of defect *D* in a supercell of size *L* (the cube root of the supercell volume) and in charge state *q*. $E^B(0,L)$ is the energy of a neutral bulk supercell of the same size as the defect supercell. n_i is the number of atoms of type *i* that were added to ($n_i > 0$) or removed from ($n_i < 0$) the bulk supercell to form the defect structure and μ_i is the chemical potential of the reservoir providing atomic exchange for atom *i*. For the case of I_P, this sum over chemical potentials is replaced by a single term, μ_P. E_F is the Fermi level defined in terms of the chemical potential of the reservoir providing electron exchange, μ_e, and a relative Fermi level, ε_F, such that $E_F \equiv \mu_e + \varepsilon_F$. Henceforth, we use the traditional convention in which μ_e is the Kohn-Sham eigenvalue at the valence-band edge, ε_{VBE}. For a given I_P configuration, the level for a transition between charge states q–1 and q is defined as the Fermi level at which the formation energies of the two charge states are equal. This can be calculated from the equation [9]

$$\Delta^D\left(q-1/q,L\right)=E_f^D\left(q-1,L,\varepsilon_{VBE}\right)-E_f^D\left(q,L,\varepsilon_{VBE}\right). \qquad (2)$$

In this LDRD project, DFT calculations were performed using the Socorro code [10] and the local-density approximation (LDA) for exchange and correlation.[2,3] Semilocal NCPs for Ga^{+3} and P^{+5} were constructed using the FHI98PP [11] code, and then converted into a local potential plus Kleinman-Bylander projectors [12] for use in Socorro. Semilocal NCP's for In^{+3} were constructed using the GNCPP [13] code of Hamann, and then converted into a local potential plus Kleinman-Bylander projectors. Non-linear core corrections [14] were used in all of the NCPs. A 30 Ryd cutoff was used to define the plane wave basis for the Kohn-Sham orbitals and the Kleinman-Bylander projectors, and a 120 Ryd cutoff was used to define the plane wave basis for the electron density and the local potentials.[15] Sampling meshes in the Brillouin zone (denoted n×n×n, where n is an integer) were constructed using the Monkhorst-Pack technique,[16] and the occupations of the Kohn-Sham orbitals at these sampling points were computed using the DFT eigenvalues and a Fermi function with $kT = 0.025852$ eV ($T = 300$K), 0.028007 eV ($T = 325$K), or 0.030161 eV ($T = 350$K).

To verify the NCPs, we performed DFT calculations for the equilibrium lattice constants of zinc blende GaP and InP in 2-atom primitive supercells using 5×5×5 Monkhorst-Pack sampling meshes. For GaP, bulk energies were calculated for twelve lattice constants ranging from 5.133 to 5.715 Å and fit using the Murnaghan equation.[17] Consistent with trends found when using the LDA, the fit yielded a cubic lattice constant of 5.387 Å, which is 0.3% smaller than the measured value at room temperature (5.405 Å).[18] For InP, bulk energies were calculated for twelve lattice constants ranging from 5.556 to 6.138 Å and fit using the Murnaghan equation.[17] Consistent with trends found when using the LDA, the fit yielded a cubic lattice constant of 5.817 Å, which is 0.9% smaller than the measured value at room temperature (5.869 Å).[19]

The phosphorus chemical potential, μ_P, needed in Eq. 1 was obtained from DFT calculations for bulk phosphorous in an orthorhombic structure using a 18×12×6 sampling mesh. The equilibrium lattice constants for this structure were found to be $a = 3.28$ Å, $b = 7.69$ A and $c = 19.09$ Å, which differ by up to 5.6% from measured values, due to our neglect of van der Waals interactions. However, they are in agreement with recent DFT results obtained using LDA exchange and correlation.[20]

2.2 DFT Calculations for I_P in InGaP

To identify relevant I_P charge states in InGaP, we performed extensive DFT studies of I_P in GaP and InP. Based on the results, we focused on three charge states; q = -1, 0 and +1. In both GaP and InP, the ground-state configurations in the -1 and 0 charge states were found to be C_{2v} 110p and the saddle-state configurations for thermally-activated hops between these configurations were found to be C_{2v} 001m. (We use the non-specific letter, m to designate either gallium or indium as the group-III atom to which the P interstitial atom is bonded.) In both GaP and InP, the ground-state configurations in the +1 charge state were found to be C_{1h} p001m, and the saddle-point configuration for thermally-activated hops between these configurations was found to be C_{2v} 110p. These three configurations are illustrated in Figure 2 for the case of GaP.

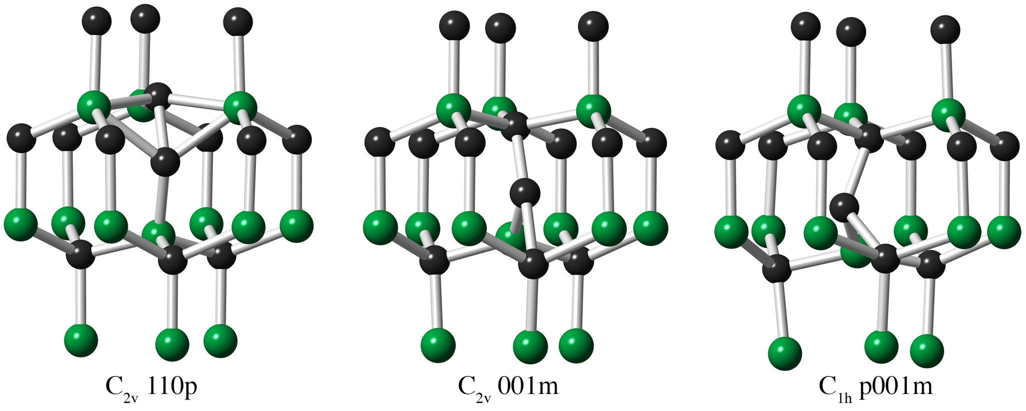

Figure 2. Ball-and-stick models of relevant I_P configurations identified in our DFT study of GaP. Green balls denote Ga atoms and black balls denote P atoms.

In the C_{2v} 110p configuration, the interstitial P atom shares a lattice site with a bulk P atom, forming a P-P dimer oriented along a <110>-type direction. In the C_{2v} 001m and C_{1h} p001m configurations, the interstitial P atom is located between two bulk P atoms and is also bonded to either a gallium or indium atom. The difference between the C_{2v} 001m and C_{1h} p001m configurations is a displacement (puckering) of the interstitial P atom off of the line between the two neighboring bulk P atoms. However, we note that because of alloy-induced symmetry breaking the C_{2v} 001m configuration in InGaP will not be the ideal one shown in Fig. 2. We further note that our KMC simulations allowed reorientation of the C_{2v} 110p and C_{1h} p001m ground-state configurations in order to enable change in the diffusion direction and thereby obtain realistic mean-squared displacements (MSDs). As in the case of diffusion, the reorientations are thermally activated. However, since the details of reorientation are less important to our studies than the diffusion itself, we did not perform explicit calculations to obtain reorientation activation energies in the alloy. Rather, we used the activation energies obtained in our study of I_P in GaP (0.34 eV for the -1 C_{2v} 110p configuration, 0.11 eV for the 0 C_{2v} 110p configuration, and 0.30 eV for the +1 C_{1h} p001m configuration) as default values and then judiciously increased these values as needed to obtain a balance between reorientation and diffusion in the alloy at a given temperature.

To determine the formation energies of I_P in InGaP, DFT calculations were performed in cubic 216-atom supercells with size L = 16.7989 Å using a 3×3×3 sampling mesh. DFT calculations for bulk InGaP and for I_P stable-states were preformed using a quenched-annealing algorithm to find the lowest-energy atomic configurations. DFT calculations for I_P saddle points were performed using the dimer method.[7] The resulting energies from each I_P supercell, $E^D(q,L)$, and its associated bulk supercell, $E^B(0,L)$, were substituted into Eq. 1 to compute the I_P formation energy. The formation energies from the training sets for each I_P charge state and configuration were then used to develop CEs for use in our KMC simulations.

3. CLUSTER EXPANSIONS

3.1 General Aspects of Cluster Expansions

The cluster-expansion (CE) formalism is a well-established approach to computing the properties of alloys.[21,22,23] In this approach, the *occupancy* of each *site* on the alloyed *sublattice* is described in terms of an Ising-like variable. For example, in the InGaP alloys that are the focus of this LDRD, this variable takes on the value +1 (–1) if a group-III site is occupied by In (Ga). The energy of the alloy is then expanded in products of these variables at the different sublattice sites. As shown in Figure 3, terms involving a single occupancy variable are called single-site (or *point) clusters*, while terms involving the product of two occupancy variables are called *pair clusters*. Terms involving the products of three occupancy variables are called *triplet clusters*, etc. In principle, the set of all clusters forms a complete and orthonormal basis for expanding any alloy property that is a function of the occupations of the sublattice sites. In practice, the expansion is truncated after a finite number of terms. The coefficients of these various terms are obtained from a least-squares fit to a *training set*. Each element of this training set consists of a point at which the desired function is known for a particular set of site occupations.

The CASM code developed by Prof. Van der Ven was used to construct our CEs.[24,25,26,27,28] In recent years, we have collaborated with Prof. Van der Ven as part of a CINT (Center for Integrated Nano-Technology) project to use the CASM code to model the surface structures of compound semiconductors.[29,30,31,32] In the general approach used in CASM, the training set is obtained from DFT calculations. In the initial stage of the CINT project, we modified CASM to work with Sandia's Socorro DFT software. A genetic algorithm was then used to optimize the set of clusters included in the expansion,[33] with the goal of minimizing a leave-one-out cross-validation score.[34]

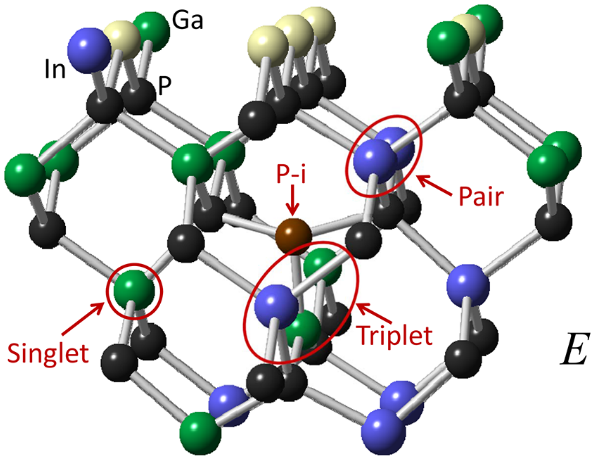

P-interstitial nearfield
C_{1h}-p001$_m$
q=+1

$$\varphi_\alpha = \prod_{i \in \alpha} \sigma_i$$

$$E(\vec{\sigma}) = E_0 + \sum_\alpha V_\alpha \cdot \varphi(\vec{\sigma})$$

Figure 3. The group-III nearfield lattice sites for the ground state of +1 C_{1h} p001m I_P in InGaP. Green and violet balls denote Ga and In group-III sites within the defect's nearfield; white balls denote other close-by group-III sites identified as having less influence on the +1 I_P formation energy that are thus designated to be in the defect's far-field; all of the more-distant group-III sites (not shown) also reside in the defined far-field.

In this LDRD project, a CE is employed to rapidly evaluate the formation energy of a particular defect in an arbitrary local alloy environment, which presents distinct technical challenges as compared to the same defect in an unalloyed environment such as in GaAs or GaP. In particular, alloying breaks the translational and rotational symmetry of the defect leading to a large number of inequivalent group-III sites. In order to produce a tractable CE, it becomes necessary to select a limited neighborhood of sites about the defect to be included in the CE (the *near-field)*. In previous LDRD work, we found a useful tool in choosing the near-field to be "*flipping calculations"* in which we used DFT to calculate the change in energy when the atom at one (alloy) site at a time was switched between Ga and In. Since the effect of flipping one site depends significantly on the occupations of the other sites, it is necessary to sample over a variety of such occupations. We then truncate our CE to include only those sites that had more significant effects in our flipping calculations. The present work on compact-model development continues to use this same approach.

This elimination of certain sites (the *far-field)* from the CE introduces another challenge: The CE must expand a well-defined function of the included variables, yet the far-field occupations introduce additional spurious fluctuations in the DFT values we were fitting. Conceptually, we overcame this obstacle by averaging the DFT results obtained with a fixed near-field over all possible *far-field* occupations. In previous work, we initially tried to perform this average by sampling over far-fields in our DFT calculations. Later in the previous LDRD project, we realized that averaging the results obtained with a given far-field with the results obtained with a "*mirrored"* far field in which all Ga atoms are replaced by In atoms, and vice versa, largely cancels the far-field effects and allows for a much more rapid and reliable evaluation of the far-field averages. Consequently, we have utilized this mirrored far-field approach when performing calculations of the InGaP-alloy defect-formation energies and saddle-point energies within the present LDRD.

3.2 Cluster Expansion of Defect Ground States and Saddle-Points in InGaP

We have constructed six CE's for the P interstitial (I_P) in an InGaP alloy. Each CE applies to a particular defect charge state and structure, and the CE can accurately predict the formation energy of this charge state and structure as a function of the local environment in the alloy. In order to simulate thermal and carrier-induced diffusion of -1, neutral, and +1 I_P, we constructed CE's for both the ground state and the transition state (saddle point) for each of these three possible charge states of the defect.

As already discussed in part in Section 2, the ground state of -1 and 0 I_P have the same split structure (see Figure 4) in which two P atoms share a single P site in the host crystal. If we do not consider symmetry breaking due to the occupations of the neighboring group-III sites in the alloy, the structure has C_{2v} symmetry, and the two P atoms of the split interstitial form a dimer oriented along a <110>-type direction. The two P atoms are indistinguishable and either one may remain at the site once the interstitial diffuses away. In contrast, the ground state of +1 I_P has a lower symmetry structure (see Figure 3) where a single interstitial P atom is positioned near (or just above, as in Figure 3) a group-III lattice site. Here, the interstitial causes a displacement (downward in Figure 3) of the metal atom such that the P and metal-atom pair share the original group-III site. In addition, there is a small rotation of the atom-pair such that the bond joining them is not directly along the vertical [001] direction. The puckered or rotation-lowered symmetry, the nominal [001] bond orientation, and the close association with a group-III metallic site, combine to give this defect its C_{1h} p001m structural designation.

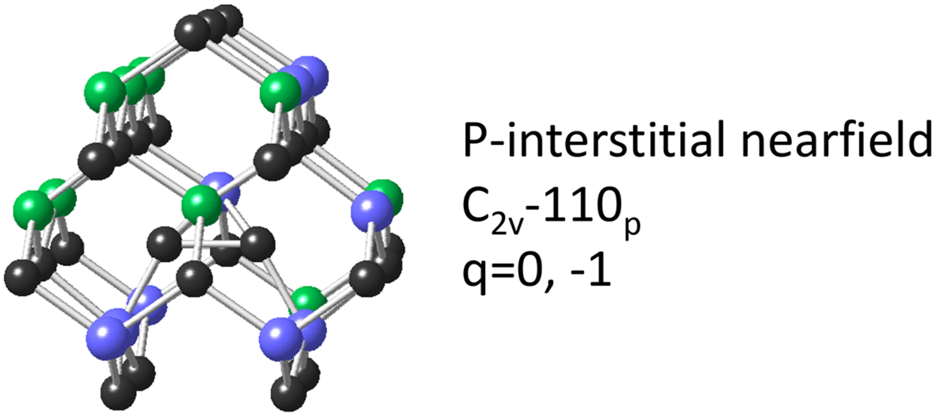

Figure 4. The group-III nearfield lattice sites for the ground states of -1 and 0 C_{2v} 110p (split-interstitial) I_P in InGaP.

For the saddle-points of the -1, 0, and +1 charge states of I_P, the structural configurations are similar to those described for the ground states, but they are essentially reversed with respect to charge state. Thus, the saddle point of +1 I_P takes on the dimerized, split-interstitial C_{2v} 110_p structure shown in Figure 4, whereas the saddle points of the -1 and 0 interstitials take on structures similar to that shown in Figure 3, but with one important difference: At the higher-energy, less-relaxed saddle points, there is a reduced puckering rotation (and in fact, there is none at all in analogous binary compounds, GaP and GaAs) such that the above-noted vertical [001] bond orientation tends to be better-preserved near the saddle point, with the nominal symmetry remaining closer to C_{2v}. The resulting structural designation for the -1 and neutral saddle points of I_P thus become C_{2v} 001_m (not shown).

Table 1 summarizes selected CE-fitting details related to each of the six types of I_P defects of interest. As seen in the table, the DFT training sets for each of the defects contained from 128 up to 152 different alloy configurations, where in each case, the defect near-field contained either 18 or 21 specific group-III sites (setting aside here the CE data for the small, preliminary 7-site near-fields noted in Table 1) arranged about the defect position, as shown above in Figure 3 and Figure 4. The defect quasi-symmetry (C_{2v} or C_{1h}), the large number of near-field sites (18 or 21), and the maximum order of the allowed CE model (triplet) combine to define the maximum number of unique configurations that may be represented by the defect's CE. In the table, the possible number of configuration ranges from 66,432 for the higher-symmetry C_{2v} defect with the smaller 18-site near-field, up to possibly 1,050,264 configurations for the lower-symmetry C_{1h} defect with the larger 21-site near-field. Thus, the DFT-training-set/cluster-expansion ansatz allows the 66,432 to 1,050,264 needed DFT calculations to be reduced to only ~152 x 2 DFT calculations (where the 2x arises from the needed mirroring).

The variance of each defect's population of formation energies, when taken about the simple mean energy of the population, ranges from 130 to 280 meV for the present six I_P states. As seen at far right in Table 1, the fitted CE representation of the alloy-site-occupancy within the defect's near-field reduces the unexplained variation in the defect energy several-fold to only 24 to 45 meV. Relative errors of this size or smaller are adequate for present first attempts to develop compact models of defect diffusion in InGaP alloys.

Table 1. Summary of Cluster-Expansion Fitting Statistics for P interstitials in InGaP. In cases where double entries appear in the table, a small nearfield (7 sites) was initially considered for exploratory purposes; this was followed by later consideration of a larger, fully populated near-field (21 sites).

InGaP P-interstitial	quasi-symmetry of defect	charge state	no. of nearfield sites	total no. of possible configs.	no. of DFT training-set configs.	no. of fitted clusters	sigma of fitted CE (eV)
➢ Ground states	C_{2v}-110_p	q =-1	18	66432	152	40	0.024
	C_{2v}-110_p	q = 0	18	66432	128	15	0.035
	C_{1h}-p001_m	q =+1	7, 21	80, 1050264	73, 152	10, 17	0.028, 0.033
➢ Saddle points	C_{2v}-001_m	q =-1	7, 21	48, 526848	48, 152	8, 16	0.029, 0.039
	C_{2v}-001_m	q = 0	7, 21	48, 526848	48, 152	10, 18	0.047, 0.045
	C_{2v}-110_p	q =+1	18	66432	143	15	0.040

As part of the work to develop these CEs for I_P, substantial additional work was done under the present LDRD to further improve the CASM-based methods for selecting the best-optimized CE for each alloy defect of interest. The chief problem that was addressed was avoidance of overfitting errors within the CASM-based cluster-expansion fitting. These errors arise in a somewhat insidious fashion because the above-described mirroring process leaves behind residual random errors in the pair-wise-averaging of the defect energies for each training-set configuration. Because the original CASM fitting algorithm was not designed to optimize properly in the presence of the mirroring errors, CASM will optimized the fit to remove the mirroring errors whenever the model has a sufficiently large number of free parameters. Notably, the *relative* random error introduced by the mirroring has been independently estimated to be roughly ±30 meV (±1σ) for the defects of interest when placed within a series of alloyed-crystal configurations of interest, whereas the underlying *relative* random error inherent in a very well-executed set of DFT defect calculations (due to k-point sampling, selection of basis-set size, and related numerical methods & details) may be as small as only a few meV.

To prevent overfitting of the mirroring errors embedded in the DFT training sets, the CASM fitting was performed in a step-wise fashion, where a series of CASM-based CE fits were performed for each defect's DFT training-set, and where the CE model complexity was incrementally increased at each step by adding an additional fitted cluster to the model. As shown in Figure 5(a), the resulting 1-sigma fitting errors of the CEs were then plotted versus the number of fitted clusters (see the blue circles, with red-line showing a fitted trend), and this plot was then compared to the independent estimate of the range of expected mirroring errors (see horizontal black-dashed lines). As shown by the colored arrows at the bottom of Figure 5, it was assumed that as the sigma of the fitted CE approaches the upper range of the expected mirroring error, increasing overfitting of the mirroring error begins to be important. The best-fitted model is assumed to rest near to this position.

To better confirm the optimal model selection, we also monitor the specific clusters selected by CASM code during the stepwise fitting of each CE model. Before the noted transition to overfitting, the ensemble of selected clusters incrementally improves in a stable, consistent fashion wherein each stepwise increase in model complexity (i. e., the number of fitted clusters) simply adds the next-most statistically important cluster to those already identified in the previous, lower-complexity steps (This stable behavior corresponds to the green-arrowed region in Figure 5(a)). At some position near to the expected transition to overfitting, the added-cluster behavior changes character, with the series of added clusters no longer offering simple, incremental improvements to an existing stable ensemble; instead, multiple clusters more randomly enter and exit as each stepwise model is fitted. This onset of clearly non-sequential cluster addition and removal with the continued stepwise model fitting, along with the simultaneous approach to the 1-sigma fitting error expected due to the mirroring, are used together to refine the choice of the best-fitted CE. The selected best-fit CE error that results for an example series of fitted models is indicated by green, coarse-dashed lines in Figure 5(a), where the optimal number of fitted clusters in the CE is 17.

Using the optimally fitted CEs, we generated histograms of the population of defect-formation energies that result for each of the cluster-expanded defects, resulting in defect-energy distributions similar to the example shown in Figure 5(b). The total range of formation energies spanned by each defect population, and the the full-width at half-maximum (FWHM) of each population, were calculated using the constructed CE histograms. These statistical measures of the energy widths of the defect-populations are discussed in a Section 4 of this report. Finally, the best-fitted CE coefficients (represented by E_0 and V_α in Figure 3) for each defect's ground state and saddle point structure were subsequently used as input parameters to our KMC simulation code. The fitted-CE representations of the DFT training sets enabled detailed KMC simulation studies of I_P diffusion in InGaP alloys. The KMC simulations and resulting compact models are described next.

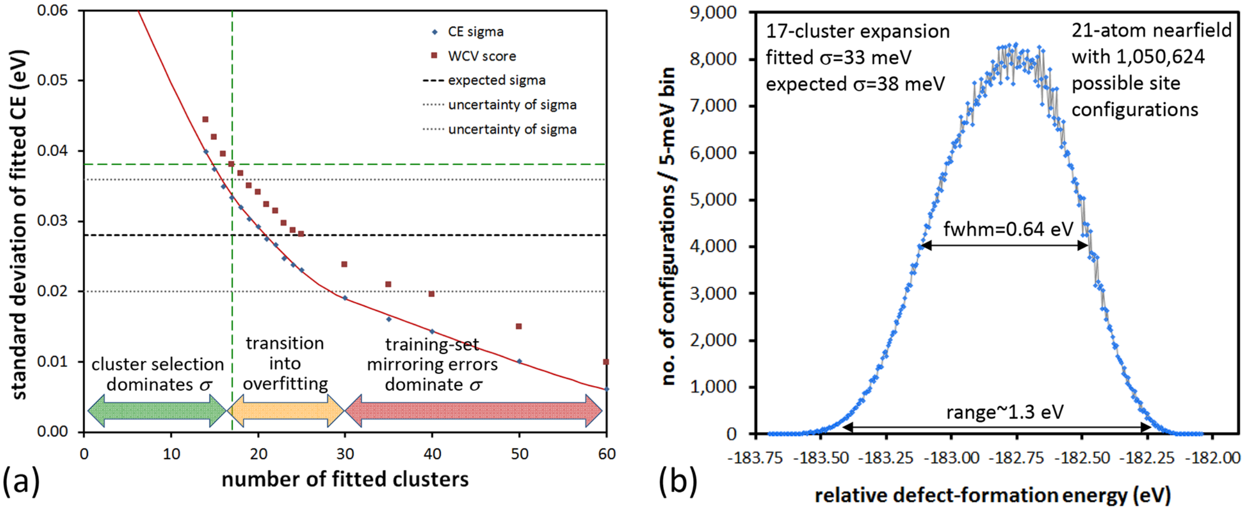

Figure 5. (a) The 1-sigma fitting error of a defect cluster expansion (CE) versus the complexity of the expansion, which is expressed as the number of fitted cluster terms. The CE was performed for the +1 C_{1h} p001m ground state of I_P in InGaP. (b) The population distribution (or histogram) of the defect-formation energies computed for the 1,050,264 possible defect-alloy configurations represented by the fitted CE.

4. KINETIC MONTE CARLO SIMULATIONS

4.1 Construction of Sub-Lattice Models for Defects in a Zinc-Blende Alloy

The first step in defining a lattice model for defect diffusion in a zinc-blende alloy is to define a physically meaningful set of lattice sites for the defect. The zinc-blende structure consists of two interpenetrating face-centered-cubic (FCC) sub-lattices. For an FCC lattice, there are 16 natural sites in each cubic unit cell: 4 atomic sites, 4 octahedral interstitial sites and 8 tetrahedral interstitial sites. In units of (*a*/4) where *a* is the cubic lattice constant, the atomic sites are (0,0,0), (0,2,2), (2,0,2) and (2,2,0). The 4 octahedral interstitial sites are obtained by adding a displacement of [2,2,2] to each of the atomic sites and the 8 tetrahedral interstitial sites are located at (±1, ±1, ±1).

To define a lattice model for zinc-blende, we denote its two FCC sub-lattices *A* and *B*. The *A* sub-lattice has its origin at (0,0,0) and the *B* sub-lattice has its origin at (1,1,1). The 4 atomic sites of the *B* sub-lattice correspond to 4 of the tetrahedral interstitial sites of the *A* sub-lattice, and the 4 octahedral interstitial sites of the *B* sub-lattice correspond to the other 4 tetrahedral interstitial sites of the *A* sub-lattice. The tetrahedral interstitial sites of the *B* sub-lattice correspond to either atomic sites or octahedral interstitial sites of the *A* sub-lattice. Therefore, a physically meaningful set of defect sites consists of the atomic sites and the octahedral interstitial sites of both the *A* and *B* sub-lattices, yielding 16 sites in the cubic unit cell. In a KMC simulation, this cubic unit cell is periodically repeated in all three directions to create a simulation cell (*system*) of the desired size.

To define a configuration of the system, species tags are assigned to the sites of the simulation cell. A defect species tag is assigned to an appropriate lattice site and bulk atom tags are assigned to the remaining atomic sites of the *A* and *B* sub-lattices. Unique defect species tags are associated with each defect charge state and structure. Since the host crystal structure (e.g., the crystal structure before species tags are assigned) is invariant with respect to a set of rotational symmetries around each lattice site, a defect with a given charge state and structure may have multiple orientations at a given lattice site. For example, the ground-state of -1 I_P is a split-interstitial structure at a bulk P site with the P-P bond oriented along one of six different <110>-type directions. The number of such orientations is determined by the symmetry of the host lattice and the symmetry of the defect. A unique species tag is associated with each of these orientations, and one of the orientations is chosen to be the reference orientation. The symmetry operations that map the reference orientation into each of the other orientations of the defect are then tabulated. Thus, the species tag for a defect codes the charge state, structure, and orientation of the defect. Using the symmetry operation associated with the species tag, any vector defined for the reference orientation can be mapped into the corresponding vector for the indicated defect.

The host crystal structure is passed in a text database to the Kinetic Monte Carlo (KMC) code. This database assigns an identification number and entity to each lattice site and provides the location of the lattice site. To facilitate the KMC simulations, the database also includes information about the atomic neighbors on the *A* and *B* sub-lattices. For each defect lattice site, the list of the identification numbers of the other lattice sites within a cut-off radius of the lattice site is pre-computed and read by the KMC code. Thus, the KMC code can readily determine the occupations of the lattice sites near the defect.

Once the KMC code has read the crystal structure database, it randomly assigns the occupation of alloyed sites (e.g., in $In_{0.5}Ga_{0.5}P$, it has a 50% chance of assigning an In species tag and a 50% chance of assigning a Ga species tag to each group-III site). The KMC code also chooses one site of an appropriate type to be a defect by assigning a defect species tag to that site, thereby fully specifying the initial system configuration for a KMC simulation. Note that this specification of the system configuration is very flexible and could be used to code systems with multiple defects, complex alloys with multiple species on each sublattice, and systems where the alloy structure changes as a result of defect diffusion. Many of these possibilities have yet to be explored.

The CEs discussed above the provide the means of calculating the formation energy of the defect ground states and saddle points for arbitrary sites and orientations in the alloy. The KMC reads each cluster expansion (CE) from a file. These files code the neighbors appearing in the CE as displacement vectors from the reference orientation defect to the neighbors. These vectors can then be mapped using the symmetry operation associated with the species tag to identify the corresponding neighbors for an arbitrary orientation of the defect. In a similar manner, each possible transition for a given defect species is coded by the displacement vectors to the transition state and the final state. These vectors are given for the reference orientation and can be mapped to other orientations using the symmetry operation associated with the species tag. By a suitable application of geometry and symmetry operations, it is possible to identify the site and orientation of the saddle point and final state for each transition.

4.2 Application of KMC to Thermal Diffusion

The KMC method provides a simple yet powerful and flexible technique for exercising the concerted action of fundamental, stochastic, physical processes to create a model of the collective behaviors they produce. In this section, we describe the application of the KMC method to thermal diffusion of -1 C_{2v} 110p I_P in InGaP. The CE introduced above for the -1 C_{2v} 110p ground state provides the means for calculating its formation energy for any system configuration, thereby allowing a *change* in its formation energy (ΔE) due to a transition from an initial configuration (initial state) to a final configuration (final state) to be calculated. Furthermore, the CEs for the ground state and the -1 C_{2v} 001m saddle-point provide the means for calculating the energy barrier (E_b) between the initial state and the final state. Using these energies, the average rate, *r*, of the transition can be expressed as

$$r = \begin{cases} A\exp\left(-\dfrac{E_b}{kT}\right) & \text{if} \quad \Delta E \le 0 \\ A\exp\left(-\dfrac{\Delta E + E_b}{kT}\right) & \text{if} \quad \Delta E > 0 \end{cases} \tag{3}$$

where *A* is half of the attempt frequency, *k* is Boltzmann's constant and *T* is the system temperature. In this work, we consider transitions involving both reorientation of the defect at a given lattice site and diffusion of the defect between lattice sites. For -1 I_P, the values for ΔE for each transition were calculated from the CE for the -1 C_{2v} 110p ground states. For diffusion, the values of E_b for each transition were calculated from the CE for the -1 C_{2v} 110p ground states and the CE for the -1 C_{2v} 001m saddle points. For reorientation, default values of E_b for each transition were taken from DFT results for I_P in GaP and then judiciously increased in order to obtain a balance between diffusion and reorientation at a given value of *T* (as previously noted in Section 2.2) during a KMC simulation. The remaining inputs to Eq. 3 were $A = 3.746\times10^{12}/2$ sec^{-1} and $kT = 0.025852$ eV ($T = 300$K), 0.028007 eV ($T = 325$K), or 0.030161 eV ($T = 350$K).

There are several KMC variants in common use today. In our work we used a kinetic adaptation[35,36,37] of the N-Fold Way,[38,39,40] which is itself a re-formulation of the Metropolis method.[41] In this approach, a list of possible transitions that the system can undergo must be maintained at all times. For the case of -1 I_P, this list consists of two diffusion events (hops) to adjacent sites along the P-P bond direction and five reorientation events in the P-P bond. At each Monte Carlo step, one event is chosen from this list such that

$$\sum_{i=1}^{m-1} r_i \leq \rho_1 \sum_{j=1}^{N} r_j < \sum_{k=1}^{m} r_k \ , \tag{4}$$

where i, j, and k are summation indices denoting the individual events, r_i is the rate of the event i, m is the index of the chosen event, N is the total number of possible events throughout the model system, and ρ_1 is a random number evenly distributed over the range [0,1). This formulation ensures that fast transitions are chosen more often than slow ones. The Monte Carlo time is then advanced by

$$\Delta t = -\frac{\ln(\rho_2)}{\sum_{j=1}^{N} r_j} , \tag{5}$$

where Δt is the time that has elapsed between the previous event, i.e. the one prior to m, and the event m itself; and ρ_2 is a random number evenly distributed over the range (0,1). After each transition is selected and executed, the lattice site occupancies of the model system are updated, and any necessary updates to the event list are made.

The ground state and transition state structures of 0 I_P are the same as for -1 I_P, and thus thermal diffusion of 0 I_P was simulated with essentially the same model used for -1 I_P with the appropriate 0 species tags and CEs. For +1 I_P, the ground states are C_{1h} p001m structures, while the transition states are approximated by the C_{2v} 110p metastable structures. In order to model the diffusion of +1 I_P, CEs for these two structures were developed and the appropriate thermal transitions were coded.

4.3 Application of KMC to Combined Thermal and Carrier-Induced Diffusion

Starting from the KMC models developed for thermal diffusion of -1, 0, and +1 I_P, a model of combined thermal and carrier-induced diffusion I_P was developed by keeping all of the states and processes in the three thermal diffusion models and adding carrier capture and emission processes that change the I_P charge state. The parameters that determine the rates of these carrier capture and emission processes are the band gap, E_G, the thermodynamic I_P levels, $E_{0,+1}$ and $E_{-1,0}$, the carrier-capture cross-sections, $\sigma_{0,+1}$ and $\sigma_{-1,0}$, the thermal velocities of holes and electrons, v_h and v_e, and the band density-of-states of holes and electrons, N^0_h and N^0_e, in InGaP In our KMC simulations, we used values for the band gap (E_G = 1.86 eV), the thermodynamic defect levels ($E_{0,+1}$ = 0.93 eV and $E_{-1,0}$ = 0.93 eV), the thermal velocities (v_h = 2.7x10^7 cm/s and v_h = 3.6x10^7 cm/s) and the density-of-states (N^0_h = 1.16x10^{19} cm^{-3} and N^0_e = 6.55x10^{17} cm^{-3}) that are consistent with the values used in recent device simulations at Sandia.[42] For the carrier-capture cross-sections, we used representative values of 10^{-16} cm^2. The densities of holes N_h and electrons N_e could then be varied along with the temperature T to model different conditions of the system. The transition rate from charge state q to charge state $q+1$ was given by

$$\boldsymbol{r} = \mathrm{N_h v_h \sigma_{q,q+1}} + \mathrm{N_e^0 v_e \sigma_{q,q+1}} \exp\left(-\frac{\left(\mathrm{E_G} - \mathrm{E_{q,q+1}}\right)}{\mathrm{kT}}\right), \tag{6}$$

where the first term corresponds to capture of holes and the second term corresponds to emission of electrons. Likewise, the transition rate from charge state *q+1* to charge state *q* was given by

$$\mathrm{r} = \mathrm{N_e v_e \sigma_{q,q+1}} + \mathrm{N_h^0 v_h \sigma_{q,q+1}} \exp\left(-\frac{\mathrm{E_{q,q+1}}}{\mathrm{kT}}\right), \tag{7}$$

where the first term corresponds to capture of electrons and the second term corresponds to emission of holes.

Alternatively, we could have used the defect levels determined from the cluster expanded energies of the initial and final states to evaluate the defect levels occurring in the carrier emission rates. This would have required a method of aligning the energy differences determined from the cluster expansions to the band edges of InGaP. This approach would be likely to produce a more accurate model of diffusion at low carrier densities (where carrier emission is significant) and would be a useful topic for future research. In addition, when a transition between different charge states occurs, it is necessary to pick a final state for the transition. Since there is a one-to-one correspondence between the sites, structures, and orientations for the -1 and 0 charge states, it is logical to assume that transitions between these charge states result in the corresponding structure of the other charge state. However, no such correspondence exists between the 0 and +1 charge states. For transitions between these charge states, we assumed that the final state is the lowest energy neighboring structure. The accuracy of this assumption depends on details of the carrier capture and emission processes, which are the subject of ongoing research. Given that the choice of final states for these processes could have significant effects on the calculated diffusion rates, especially at higher carrier concentrations in which the current approach leads to an absence of sustained Bourgoin-Corbett diffusion in the alloy, future research in this area would be worthwhile.

4.4 KMC for Thermal Diffusion of I_P in InGaP

The KMC application described in Section 4.2 was utilized to simulate thermal diffusion of -1, 0 and +1 I_P in an InGaP alloy using the CEs described in Section 3. The simulations tracked 2304 diffusion histories for run times of up to 96 hours. After a run, the Mean-Squared-Displacements (MSDs) of the histories were averaged and the averages plotted as a function of the (diffusion) time. As noted in the introduction, general aspects of these plots were discussed in a previous LDRD report by us.[43] Briefly, there is an initial transient during which the slope (the diffusion rate) is close to the value that would be obtained with an activation energy equal to the difference in the average energies of the saddle-point and ground-state CEs. Followed this transient, the diffusion rate reaches a steady-state value that is lower than the diffusion rate during the initial transient. Analysis of the steady-state process reveals that it is trap-mediated diffusion. The steady-state diffusion rates will be our main concern in the discussions below and will constitute the compact models extracted for use in Sandia device modeling codes.

Figure 6 shows a plot of MSD vs. Time for thermal diffusion of the -1 charge state from a 96-hour KMC simulation at $T = 300$K. In the plot, the initial transient is followed by a large decrease in the diffusion rate to a steady-state value. To extract the steady-state diffusion rate, we computed the change in the MSD over the interval from $t = 150$ to t = 200 sec, obtaining a value of 0.07477 nm^2/sec. As a check of this result, we estimated an effective activation energy for the steady-state diffusion rate using the expression

$$\Delta MSD = 6D\Delta t. \tag{8}$$

In this expression, ΔMSD is the change in the MSD from Figure 6 (0.07477 nm^2), Δt is the time interval of the change (50 sec), and D the diffusion coefficient,

$$D = D_0 \exp(E/kT). \tag{9}$$

For the prefactor, D_0, we take the value used in a Sandia device modelling code, 10^{11} nm^2/sec. Substituting, Eq. 9 into Eq. 8 and using $kT = 0.025852$ eV, we found a value of 0.87 eV for the activation energy. This value is 0.15 eV higher than the difference in the average energies of the saddle-point and ground-state CEs (0.72 eV). In addition, it is close to the 0.92 eV found in experimental studies of annealing of radiation damage in the *n*-type InGaP region of a Sandia heterojunction bipolar transistor.[44]

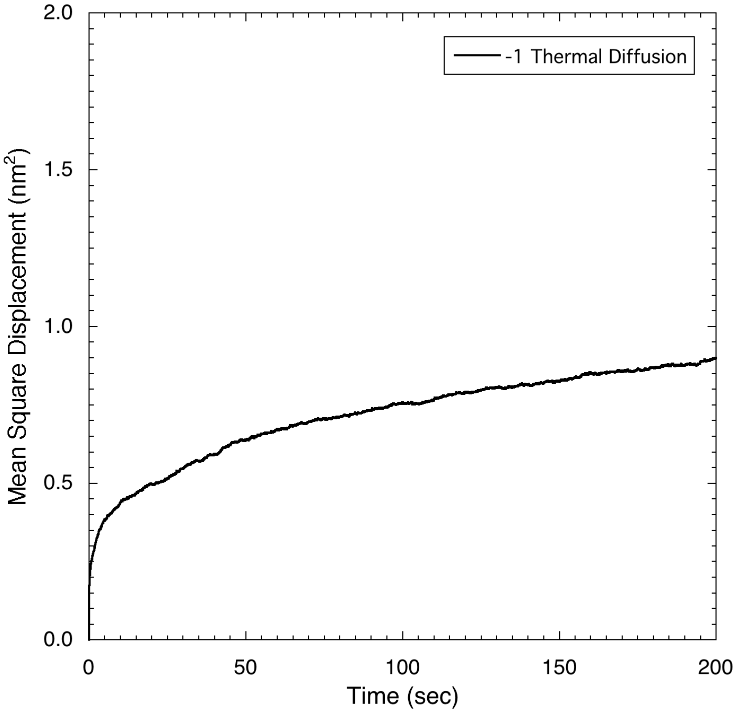

Figure 6. Plot of MSD vs. Time for thermal diffusion of -1 I_P in InGaP at T = 300K.

Fig. 7 shows plots of MSD vs. Time for thermal diffusion of the -1, 0, and +1 charge states at *T* = 300K. The steady-state diffusion rate of 0 I_P is significantly higher than the steady-state diffusion rates of -1 and +1$_P$. Estimating an effective activation energy for the steady-state diffusion rate of 0 I_P yields the value 0.56 eV, which is 0.11 eV higher than the difference in the average energies of the saddle-point and ground-state CEs (0.45 eV). This suggests that the 0 I_P undergoes less trapping than -1 (and +1) I_P in the steady-state regime. We further note that this result correlates with the 0.15 eV narrower FWHM of the ground-state CE energy distribution for the 0 charge state (0.50 eV) compared with the FWHM of the ground-state CE energies for the -1 and +1 charge states (0.65 eV). Further study will be needed to better understand and quantify the effects of trapping and their dependence on charge state.

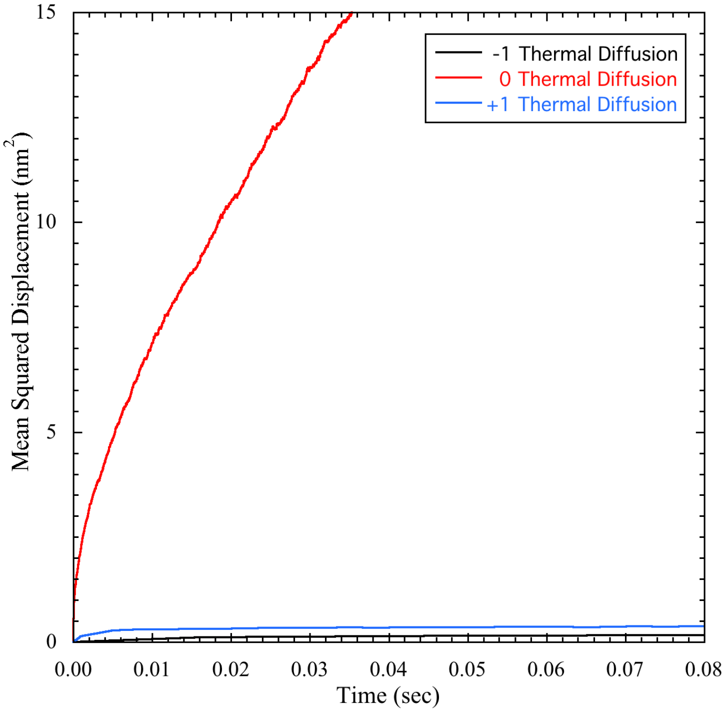

Figure 7. Plots of MSD vs. Time for thermal diffusion of -1, 0, and +1 I_P in InGaP at *T* = 300K.

4.5 KMC for Combined Thermal and Carrier-Induced Diffusion of I_P in InGaP

The KMC application described in Section 4.3 was utilized to simulate combined thermal and carrier-induced diffusion of I_P in an InGaP alloy using the CEs described in Section 3. The simulations tracked 2304 diffusion histories for run times of up to 48 hours. After a run, the Mean-Squared-Displacements (MSDs) of the histories were averaged and the averages plotted as a function of the (diffusion) time. Fig. 8 repeats the plots of MSD vs. Time for thermal diffusion of the -1, 0, and +1 charge states at *T* = 300K shown in Fig 7, and adds a plot of MSD vs. Time for carrier-induced diffusion of I_P at 300K with a carrier density of 10^{12} cm^{-3}. The diffusion rate of I_P with carriers is greater than those of -1 and +1 I_P, but less than that of 0 I_P. The interpretation of these results is that the presence of carriers leads to a non-zero population of 0 I_P having a higher diffusion rate than -1 and +1 I_P.

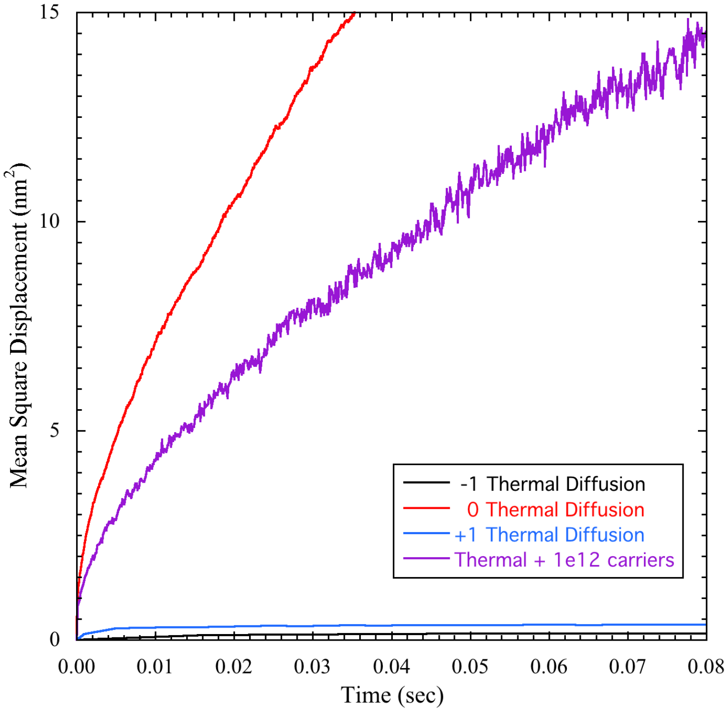

Figure 8. Plots of MSD vs. Time for thermal diffusion of -1, 0, and +1 I_P in InGaP at *T* = 300K and combined thermal and carrier-induced diffusion of I_P at *T* = 300K with a carrier density of 10^{12} cm^{-3}.

This interpretation is confirmed by increasing the carrier density to 10^{14} cm^{-3} (Fig. 9). The carrier-induced diffusion rate of I_P is noticeably increased, indicating that the steady-state population of 0 I_P is increased, approaching the thermal diffusion rate of 0 I_P. The steady-state diffusion rate for I_P undergoing combined thermal and carrier-induced diffusion can then be extracted using the same procedures outlined above and utilized in Sandia device modeling codes to model I_P diffusion and the resulting annealing of radiation damage.

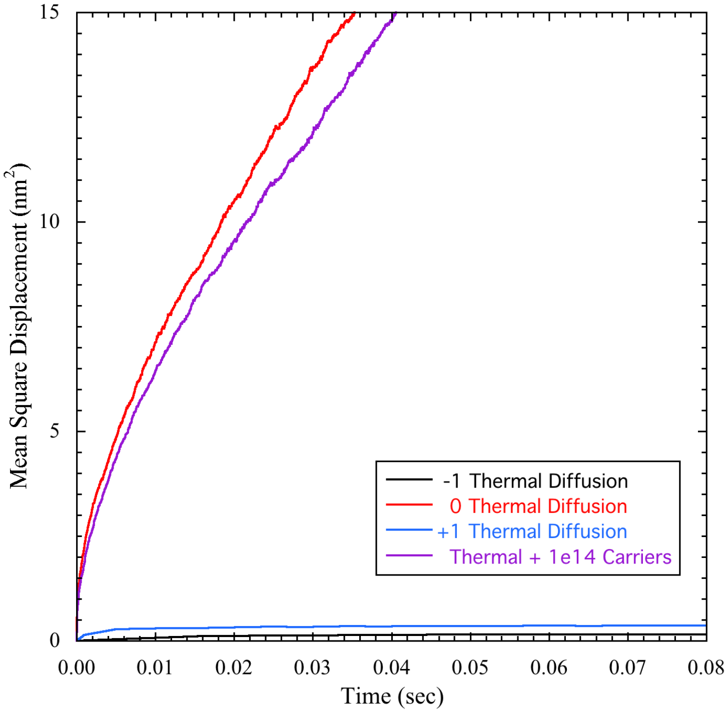

Figure 9. Plots of MSD vs. Time for thermal diffusion of -1, 0, and +1 I_P in InGaP at *T* = 300K and combined thermal and carrier-induced diffusion of I_P at *T* = 300K with a carrier density of 10^{14} cm^{-3}.

5. CONCLUSIONS

This project has significantly expanded a theoretical capability that was developed in a previous LDRD project by: (1) refining the development of cluster expansions so as to remove far-field effects and increase the accuracy of the expansions, (2) developing a new capability for KMC simulations of combined thermal and carrier-induced diffusion of defects in alloys, and (3) developing compact models that can be employed in Sandia device modeling codes to accurately model the annealing rate of radiation damage in radiation-hard devices containing alloys. This expanded capability was demonstrated by performing KMC simulations of thermal diffusion and combined thermal and carrier-induced diffusion of a P interstitial (I_P) in an $In_{0.5}Ga_{0.5}P$ alloy, which is currently used in the n-type emitter of a Sandia radiation-hard transistor, and extracting compact models of the steady-state diffusion rates for use in simulations for this device. More broadly, this capability, and the expertise to employ it, effectively enable the increased use of alloys in future radiation-hard devices, thereby increasing confidence in qualification evidence obtained from device simulations.

REFERENCES

---

[1] P. Hohenberg and W. Kohn, *Inhomogeneous Electron Gas*, Physical Review **136**, B 864 (1964).

[2] W. Kohn and L. J. Sham, *Self-Consistent Equations Including Exchange and Correlation Effects*, Physical Review **140**, A 1133 (1965).

[3] D. M. Ceperley and B. J. Alder, *Ground State of the Electron Gas by a Stochastic Method*, Physical Review Letters **45**, 566 (1980).

[4] J. P. Perdew and Y. Wang, *Accurate and Simple analytic representation of the electron-gas correlation energy*, Physical Review B **45**, 13244 (1992).

[5] D. R. Hamann, M. Schülter, and C. Chiang, *Norm-conserving pseudpotentials*, Physical Review Letters **43**, 1494 (1979).

[6] Y. Bar-Yam and J. D. Joannopoulos, *Electronic structure and total-energy migration barriers of silicon self-interstitials*, Physical Review B **30**, 1844 (1984).

[7] G. Henkelman and H. Jonsson, *The dimer method for finding saddle points on high dimensional potential surfaces using only first derivatives*, Journal of Chemical Physics **111**, 7010 (1999).

[8] S. B. Zhang and J. E. Northrup, *Chemical potential dependence of defect formation energies in GaAs: Application to Ga self-diffusion*, Physical Review Letters **67**, 2339 (1991).

[9] C. Freysoldt, B. Grabowski, T. Hickel, J. Neugebauer, G. Kresse, A. Janotti, and C. G. Van de Walle, *First-principles calculations for point defects in solids*, Reviews of Modern Physics **86**, 253 (2014).

[10] http://dft.sandia.gov/socorro.

[11] http://www.fhi-berlin.mpg.de/th/fhi98PP/. Three electrons were treated as valence ($4s_2$ and $4p_1$) for Ga and five electrons ($4s_2$ and $4p_3$) for As. Cutoff radii of 1.10, 1.30, and 2.25 Bohr were used for the *s*, *p*, and *d* channels of Ga and 1.00, 1.18, and 1.80 Bohr were used for As. Radii of 1.20 and 1.00 Bohr were used for Ga and As, respectively, to generate the partial core charges.

[12] L. Kleinman and D. M. Bylander, *Efficacious Form for Model Pseudopotentials*, Physical Review Letters **48**, 1445 (1982). The projectors were constructed using the *s* semilocal NCP as the local potential.

[13] D. R. Hamann, *Generalized norm-conserving pseudopotentials*, Physical Review B **40**, 2980 (1989). Three electrons were treated as valence ($5s_2$ and $5p_1$). Cutoff radii of 1.26, 1.40, 1.87, and 1.10 Bohr were used for the *s*, *p*, *d* and *f* channels. A radius of 1.80 Bohr was used to generate the partial core charge.

[14] S.G. Louie, S. Froyen, and M. L. Cohen, *Nonlinear ionic pseudopotentials in spin-density-functional calculations*, Physical Review B **26**, 1738 (1982).

[15] J. Ihm, A. Zunger, and M. L. Cohen, *Momentum-space formalism for the total energy of solids*, Journal of Physics C **12**, 4409 (1979).

[16] H. J. Monkhorst and J. D. Pack, *Special points for Brillouin-zone integrations*, Physical Review B **13**, 5188 (1976).

[17] F. D. Murnaghan, *The Compressibility of Media under Extreme Pressures*, Proc. Natl. Acad. Sci. U.S.A. **30**, 244 (1944).

[18] O. Madelung (Editor), *Semiconductors - Basic Data*, 2nd Edition, (Springer-Verlag, Berlin, 1996), p. 95.

[19] O. Madelung (Editor), *Semiconductors - Basic Data*, 2nd Edition, (Springer-Verlag, Berlin, 1996), p. 127.

[20] S. Appalakondaiah, G. Vaitheeswaran, S. Lebegue, N. E. Christensen, and A. Svane, *Effect of van der Waals interactions on the structural and elastic properties of black phosphorus*, Physical Review B **86**, 035105 (2012).

[21] J. M. Sanchez, F. Ducastelle, and D. Gratias, Physica A: Statistical and Theoretical Physics **128**, 334 (1984).

---

[22] D. De Fontaine, in *Solid State Physics*, edited by H. Ehrenreich and D. Turnbull (Academic, New York, 1994), p. 33.

[23] A. Zunger, in *Statics and Dynamics of Alloy Phase Transformations*, NATO Advanced Studies Institute, Series B: Physics, Vol. 319, edited by P. E. A. Turchi and A. Gonia (Plenum, New York, 1992), p. 361.

[24] A. Van der Ven, J.C. Thomas, and Q. Xu, Phys. Rev. B **78**, 104306 (2008).

[25] Q. Xu and A. Van der Ven, Intermetallics **17**, 319 (2009).

[26] Q. Xu and A. Van der Ven, Phys. Rev. B **81**, 064303 (2010).

[27] A. Van der Ven, H.-C. Yu, G. Ceder, and K. Thornton, Progress in Mater. Sci. **55**, 61 (2010).

[28] J. Bhattacharya and A. Van der Ven, Phys. Rev. B **83**, 144302(2011).

[29] J.C. Thomas, J. Mirecki Millunchick, N. A. Modine, and A. Van der Ven, Phys. Rev. B **80**, 125315 (2009).

[30] J.C. Thomas, N. A. Modine, J. Mirecki Millunchick, and A. Van der Ven, Phys. Rev. B **82**, 165434 (2010).

[31] J.C. Thomas, A. Van der Ven, J. Mirecki Millunchick, and N. A. Modine, Phys. Rev. B **87**, 075320 (2013).

[32] J.C. Thomas, J. Mirecki Millunchick, A. Van der Ven, and N. A. Modine, Phys. Rev. B **89**, 205306 (2014).

[33] G. Hart, V. Blum, M. Walorski, and A. Zunger, Nature Mater. **4**, 391 (2005).

[34] A. van de Walle and G. Ceder, J. Phase Equilib. **23**, 348 (2002).

[35] A. F. Voter. *Classically exact overlayer dynamics: diffusion of rhodium clusters on Rh(100)*, Phys. Rev. B, **34**, 6819 (1986).

[36] G. N. Hassold and E. A. Holm. *A fast serial algorithm for the finite temperature quenched Potts model*, Computers in Physics **7**, 97 (1993).

[37] C. C. Battaile, D. J. Srolovitz, and J. E. Butler. *A kinetic Monte Carlo method for the atomistic simulation of chemical vapor deposition: Application to diamond*, J. Appl. Phys. **82**, 6293 (1997).

[38] A. B. Bortz, M. H. Kalos, and J. L. Lebowitz, *A new algorithm for Monte Carlo simulation of Ising spin systems*, J. Comp. Phys. **17**, 10 (1975).

[39] D. T. Gillespiem *Exact stochastic simulation of coupled chemical reactions*, J. Phys. Chem. 81, 2340 (1977).

[40] K. A. Fichthorn and W. H. Weinberg, *Theoretical foundations of dynamical Monte Carlo simulations*, J. Chem. Phys. **95** 1090 (1991).

[41] N. Metropolis, A. W. Rosenbluth, M. N. Rosenbluth, A. H. Teller, and E. Teller, *Equation of state calculations by fast computing machines*, J. Chem. Phys. **21**, 1087 (1953).

[41] N. Metropolis, A. W. Rosenbluth, M. N. Rosenbluth, A. H. Teller, and E. Teller, *Equation of state calculations by fast computing machines*, J. Chem. Phys. **21**, 1087 (1953).

[42] S. M. Myers, W. R. Wampler, and N. A. Modine, *Recombination by band-to-defect tunneling near semiconductor heterojunctions: A theoretical model*, J. Appl. Phys. **120**, 134502 (2016).

[43] A. F. Wright, N. A. Modine, S. R. Lee, S. M. Foiles, and C. C. Battaile, *A New Capability to Model Defects in InGaAs and InGaP Alloys*, SAND2014-17844 (2014).

[44] Private Communication (W. R. Wampler).

DISTRIBUTION

1	MS0359	D. Chavez, LDRD Office	1171
1	MS1086	Stephen R. Lee	1876
1	MS1179	Leonard Lorence	1341
1	MS1315	Normand A. Modine	1881
1	MS1411	Stephen M. Foiles	1814
1	MS1415	Alan F. Wright	1881
1	MS0899	Technical Library	10756 (electronic copy)